Pergamon

Int. J. Heat Mass Transfer. Vol. 37, No. 16, pp. 2439–2463, 1994

0017–9310/94 $7.00 + 0.00

0017–9310(94)E0079–A

Buoyancy-induced convection from isothermal L-shaped corners with symmetrically heated surfaces

D. ANGIRASA, R. B. CHINNAKOTLA and R. L. MAHAJAN
Department of Mechanical Engineering, University of Colorado, Boulder, CO 80309-0427, U.S.A.

(*Received* 11 *June* 1993 *and in final form* 4 *March* 1994)

Abstract—A numerical study of buoyancy-driven transport from an isothermal symmetrically heated L-shaped corner is reported. The effect of the length of the heated horizontal surface on heat transfer from the vertical surface and the concomitant complex changes in the entrainment flow characteristics are discussed. Results are reported for a wide range of Rayleigh number. The unsteady laminar flows at high Rayleigh numbers exhibit interesting interactions between the horizontal and vertical entrainment flows. Their transient behavior is investigated in detail. The effect of Prandtl number, independent of Rayleigh number, is shown to be significant. In the lower Rayleigh number range, the Nusselt number for each surface of the L-corner is compared with the Nusselt number for the corresponding single surface. The underlying basic physical processes are discussed. Steady and transient Nusselt number data are provided.

1. INTRODUCTION

BUOYANCY-INDUCED convective transport from corners with different wall and ambient conditions is encountered in many applications. The flow and heat transfer from the combined surfaces of a corner are quite different from those of the individual surfaces. Interesting interactive flows arise. Angirasa and Mahajan [1] reviewed such flows, and classified corners based on their orientation with each other and with the gravity vector.

In this paper, we study the convective transport in a right angle horizontal corner (L-shaped) of the type shown in Fig. 1. Rodighiero and de Socio [2] reported experimental studies in air for L-shaped corners consisting of an isothermal heated vertical wall and adiabatic horizontal walls. They obtained heat transfer rates which are lower than those for a single heated vertical plate. Angirasa and Mahajan [1] studied the problem numerically in detail. The results indicated that the reduced heat transfer is due to the blockage of entrainment from the bottom side. They also studied the effect of short protrusions at the leading edge which led to the determination of a critical length for the horizontal adiabatic surface, beyond which its length has no effect on the heat transfer rate from the vertical surface of the corner. The entrainment flow, however, was shown to change significantly with the length of the horizontal side. In both refs [1] and [2], Nusselt number correlations for large horizontal adiabatic walls were reported that agreed well with each other.

Ingham and Pop [3] studied the higher order effects on the vertical boundary layer using the method of asymptotic matched expansions. In this study, the vertical surface had constant heat flux condition and the horizontal surface was maintained as adiabatic. Ingham and Pop [4] also studied a horizontal corner with an arbitrary angle between the two surfaces, with the horizontal surface hot isothermal and the other adiabatic. In a later study [5], they presented a higher order analysis for a right-angle corner with the vertical wall insulated, and the horizontal surface maintained at a constant heat flux.

Jaluria [6] numerically studied the interaction of natural convection wakes arising from two line thermal sources mounted on a vertical adiabatic surface with a cold isothermal wall forming the horizontal surface of an L-shaped corner. One of the line heat sources is aligned with the corner, and hence the horizontal wall absorbs heat from it. This heat removal reduces the buoyancy. The horizontal plate is also

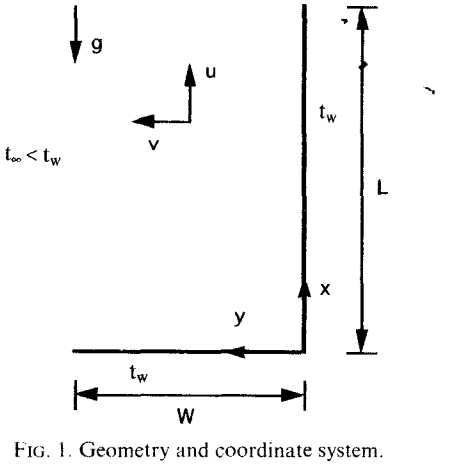

FIG. 1. Geometry and coordinate system.

NOMENCLATURE

g	gravitational acceleration
Gr	Grashof number, $= g\beta(t_w - t_\infty)L^3/\nu^2$
k	thermal conductivity of the fluid
L	height of the vertical surface of the corner
Nu_h	average Nusselt number for horizontal plate
Nu_L	average Nusselt number for the isothermal L-shaped corner
Nu_{sh}	average Nusselt number for single horizontal plate
Nu_{sv}	average Nusselt number for single vertical plate
Nu_v	average Nusselt number for vertical plate
p	pressure
P	non-dimensional pressure, $= p/\rho U_c^2$
Pr	Prandtl number, $= \nu/\alpha$
t	temperature
t_w	wall temperature
t_∞	ambient temperature
T	non-dimensional temperature, $= (t - t_\infty)/(t_w - t_\infty)$
u	velocity component in the x-direction
U_c	reference convective velocity, $= \sqrt{[g\beta(t_w - t_\infty)L]}$
U	non-dimensional velocity component in the x-direction, $= u/U_c$
v	velocity component in the y-direction
V	non-dimensional velocity component in the y-direction, $= v/U_c$
W	length of the horizontal surface of the corner
W^*	non-dimensional length of the horizontal plate, $= W/L$
x, y	space coordinates in the vertical and horizontal directions, respectively
X, Y	non-dimensional space coordinates.

Greek symbols

α	thermal diffusivity
β	coefficient of thermal expansion $= -(1/\rho)(\partial\rho/\partial t)_p$
ν	kinematic viscosity
ρ	density
τ	time
τ^*	non-dimensional time, $= \tau U_c/L$
ψ	stream function
ω	vorticity

shown to block entrainment. In their study of L-shaped corners, Angirasa and Mahajan [1] also reported results for the horizontal leg held isothermal at the ambient temperature. It was shown that for this case the Nusselt number of the vertical wall was slightly higher than when the horizontal surface was adiabatic. Luchini [7] studied the horizontal corner formed with a vertical hot isothermal plate and a cold isothermal plate joined at various angles between them. The method of matched asymptotic expansions was used, and numerical solutions were obtained by a finite-difference method. There was wide disagreement between analytical and numerical predictions of skin friction. No heat transfer results were given.

For a horizontal corner with both surfaces heated, the experimental study of Ruiz and Sparrow [8] is significant. They reported measurements of heat transfer from isothermal square grooves (V-shaped) and horizontal corners (L-shaped). A higher range of Rayleigh number ($0.3 \times 10^7 < Ra < 0.5 \times 10^9$) was considered, and the end effects were studied in detail. In the range of Rayleigh number considered, the flow visualization indicated that the flow was essentially turbulent.

In this paper, we report a comprehensive numerical study of isothermal L-shaped corners for laminar flow. The length of the horizontal side is varied from small protrusions to twice the height of the vertical side. For square corners, different Rayleigh numbers are considered. For some of the parameters, the transport is unsteady or periodic. Their time histories are investigated in detail. The underlying physical processes of these complex flows are explained. Complete Nusselt number data are presented for the horizontal and vertical surfaces of the corner individually, and also for the corner.

2. ANALYSIS

The corner configuration is shown in Fig. 1, where the height of the vertical surface is L and the length of the horizontal surface is W. The vertical and horizontal surfaces are aligned with the x- and y-directions, respectively. Both the surfaces are isothermal at t_w, which is above the ambient fluid temperature, t_∞. Using the Boussinesq approximation, the governing equations in non-dimensional form for laminar, two-dimensional, incompressible buoyancy-driven flows with constant fluid properties are

$$\frac{\partial U}{\partial X} + \frac{\partial V}{\partial Y} = 0 \tag{1}$$

$$\frac{\partial U}{\partial \tau^*} + U\frac{\partial U}{\partial X} + V\frac{\partial U}{\partial Y} = -\frac{\partial P}{\partial X} + \frac{1}{\sqrt{Gr}}\left[\frac{\partial^2 U}{\partial X^2} + \frac{\partial^2 U}{\partial Y^2}\right] + T \tag{2}$$

$$\frac{\partial V}{\partial \tau^*} + U\frac{\partial V}{\partial X} + V\frac{\partial V}{\partial Y} = -\frac{\partial P}{\partial Y} + \frac{1}{\sqrt{Gr}}\left[\frac{\partial^2 V}{\partial X^2} + \frac{\partial^2 V}{\partial Y^2}\right] \tag{3}$$

$$\frac{\partial T}{\partial \tau^*} + U\frac{\partial T}{\partial X} + V\frac{\partial T}{\partial Y} = \frac{1}{\sqrt{Gr}\,Pr}\left[\frac{\partial^2 T}{\partial X^2} + \frac{\partial^2 T}{\partial Y^2}\right], \tag{4}$$

where $P = p/\rho U_c^2$ is the non-dimensional pressure,

$$Gr = \left[\frac{g\beta(t_w - t_\infty)L^3}{\upsilon^2}\right]$$

is the Grashof number and $Pr = \upsilon/\alpha$ the Prandtl number. The transient terms in equations (2)–(4) are retained in anticipation of unsteady flows. When steady-state flows exist, the transient discretized equations can be marched to asymptotic steady-state solutions.

In deriving equations (1)–(4) from the dimensional form (see, for instance, Gebhart *et al.* [9]), the following non-dimensional terms were defined:

$$X = x/L \quad Y = y/L \quad \tau^* = \tau U_c/L$$
$$U = u/U_c \quad V = v/U_c \quad T = (t - t_\infty)/(t_w - t_\infty), \tag{5}$$

where U_c is the reference convective velocity and is given by $\sqrt{[g\beta(t_w - t_\infty)L]}$. The governing equations (1)–(3) can be reduced to a vorticity–transport equation by defining vorticity as

$$\omega = \frac{\partial U}{\partial Y} - \frac{\partial V}{\partial X}. \tag{6}$$

The subsequent vorticity–transport equation is

$$\frac{\partial \omega}{\partial \tau^*} + U\frac{\partial \omega}{\partial X} + V\frac{\partial \omega}{\partial Y} = \frac{\partial T}{\partial Y} + \frac{1}{\sqrt{Gr}}\left[\frac{\partial^2 \omega}{\partial X^2} + \frac{\partial^2 \omega}{\partial Y^2}\right]. \tag{7}$$

A stream function Ψ is defined such that

$$U = \partial\Psi/\partial Y \quad \text{and} \quad V = -\partial\Psi/\partial X. \tag{8}$$

From equations (6) and (8), it follows that

$$\omega = \nabla^2\Psi. \tag{9}$$

Boundary conditions

The physical boundary conditions of the L-shaped corner are

$$y = 0 \quad t = t_w \quad u = 0 \quad v = 0$$
$$y \to \infty \quad t = t_\infty \quad u = 0$$
$$x = 0 \quad 0 \leqslant y \leqslant W: \quad u = 0 \quad v = 0 \quad t = t_w. \tag{10}$$

The boundary conditions, in non-dimensional form, are given as

$$Y = 0 \quad T = 1 \quad U = 0 \quad V = 0$$
$$Y \to \infty \quad T = 0 \quad U = 0$$
$$X = 0 \quad 0 \leqslant Y \leqslant W^*: \quad U = 0 \quad V = 0 \quad T = 1, \tag{11}$$

where $W^* = W/L$. Numerical boundary conditions for Ψ and ω will be given in the next section.

Evaluation of Nusselt number

The average Nusselt numbers for the heated isothermal vertical and horizontal surfaces of the L-corner, respectively, are given by

$$Nu_v = \int_0^1 \left[-\frac{\partial T}{\partial Y}\right]_{Y=0} \mathrm{d}X \tag{12}$$

$$Nu_h = \int_0^{W^*} \left[-\frac{\partial T}{\partial X}\right]_{X=0} \mathrm{d}Y. \tag{13}$$

The average Nusselt number for the L-shaped corner is given by

$$Nu_L = (Nu_v + Nu_h)/(1 + W^*). \tag{14}$$

3. NUMERICAL PROCEDURE

The Alternating Direction Implicit method (ADI) of Peaceman and Rachford (see Roache [10]) is used to solve the energy and vorticity–transport equations (4) and (7). Upwind-differencing is used for convective terms for numerical stability. The diffusive and buoyancy terms are discretized by central-differencing. The stream function equation (9) is solved by the Successive Over Relaxation (SOR) method [10]. Iterative convergence is obtained for stream function solution at each time step.

The following criteria are used to check for steady-state:

$$|\xi_{ij}^{n+1} - \xi_{ij}^n|_{\max} \leqslant \varepsilon \quad \text{and} \quad \left|\frac{\xi_{ij}^{n+1} - \xi_{ij}^n}{\xi_{ij}^n}\right|_{\max} \leqslant \varepsilon,$$

where ξ is T and ω, n is time, and i and j are space coordinates. The value of ε is taken to be 10^{-5}. It was found that the temperature field converges faster than the flow field. The same type of iterative convergence test was carried out for Ψ at each time step. The non-dimensional time step chosen is of the order of 0.005.

Simpson's rule is used to evaluate the average Nusselt number, equations (12) and (13). An open-ended formula has been employed to account for the effect of end-points (see Press *et al.* [11]).

Computational domain

For an L-shaped corner with an adiabatic or cold isothermal horizontal wall, Angirasa and Mahajan [1] demonstrated that a rectangle formed with the two sides of the corner is sufficient as the computational domain to obtain accurate solutions if the length of the horizontal side is larger than the boundary layer thickness on the vertical leg. The effect of the computational domain for the heated corner is shown in Table 1 with the computational domain in the Y-direction taken as equal to W^*, $2W^*$ and $3W^*$. For $W^* = 1.0$ and $Ra = 0.7 \times 10^6$, the results clearly indicate the need for an extended computational domain

Table 1. $Ra = 0.7 \times 10^6$, W* = 1.0

	Truncated domain	Extended domain	
	$Y_{max} = W^*$	$Y_{max} = 2W^*$	$Y_{max} = 3W^*$
Nu_L	9.55	8.02	7.89

for accurate determination of the effect of the far-field on transport from the corner. An extended domain in the Y-direction twice the length of the heated horizontal surface is appropriate.

For short horizontal protrusions at the leading edge of the vertical surface ($W^* \leqslant 0.25$), the vertical boundary layer thickness is of the same order as the length of the horizontal protrusion. In this range of W^*, $Y_{max} = 0.5$ gave accurate results. For a detailed quantitative discussion on the computational domain, see Angirasa and Mahajan [1].

Numerical boundary and initial conditions

The numerical boundary conditions ($\tau^* > 0$) for both types of domain are discussed by Angirasa and Mahajan [1]. Figure 2 shows the boundary conditions for the extended domain employed in the present study. Wall vorticities are evaluated from the values of stream function at the adjacent grid points as

$$\omega_w = 2(\Psi_{w+1} - \Psi_w)/\Delta n^2, \tag{15}$$

where Δn is the grid distance normal to the wall [10]. The initial conditions are

$$\tau^* = 0 \quad \Psi = 0$$
$$\omega = 0 \quad \text{and} \quad T = 0 \quad \text{for all } X \text{ and } Y. \tag{16}$$

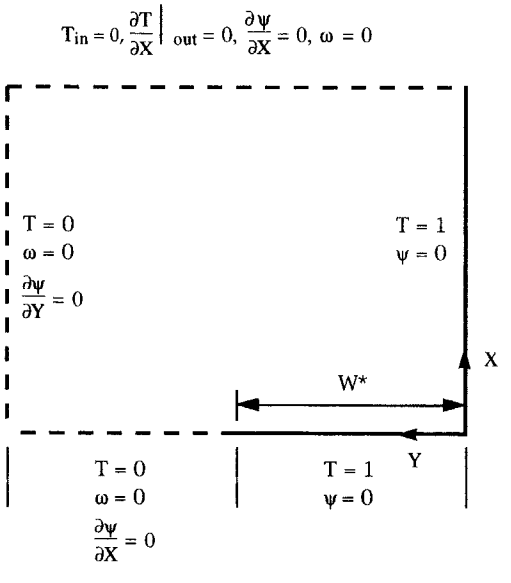

FIG. 2. Numerical boundary conditions.

Grid independence study

A series of calculations was carried out with uniform grid spacing to study the effect of the grid size on the solution. Based on this study, the number of grid points in each direction was chosen to be 81 for a square computational domain ($W^* = 0.5$ and $Y_{max} = 1.0$). For larger W^*, the grid points in the Y-direction were increased proportionately. The numerical errors associated with the grid size are assessed as less than 1% for flow and temperature fields, and 2% for Nusselt number. The error in Nu is estimated based on its asymptotic value as the grid size was decreased from 1/40 to 1/120. For the error in temperature and vorticity fields, the error estimate is based on the maximum difference of their respective values for the different grid sizes at the same location (see also ref. [1]). A larger error in Nu occurs because of the uncertainty of temperature gradients at the end-points. The combined uncertainty in Nusselt number due to grid size and domain is calculated as 2.8%.

4. RESULTS AND DISCUSSION

Steady-state solutions for moderate Rayleigh numbers

Steady-state solutions have been obtained for the Rayleigh number range of 0.7×10^4–0.7×10^6. At higher Rayleigh numbers, the solutions became either periodic or unsteady. Unsteady solutions and the effect of Prandtl number will be considered in a subsequent section.

Effect of W* *on flow and heat transfer.* Results are presented for $Ra = 0.7 \times 10^6$ and $Pr = 0.7$ for W^* varying between 0.0 and 2.0, where $W^* = 0.0$ refers to a single flat vertical surface. A comparison of our computed value of Nu for $W^* = 0.0$ with those in the literature (Table 2) shows good agreement.

Figure 3 shows the stream function contours for W^* varying between 0.1 and 2.0. The buoyancy-induced flow adjacent to a single flat vertical surface entrains fluid from the side and from the bottom (see, for instance, ref. [1]). It was shown in ref. [1] that the presence of short adiabatic protrusions at the leading edge blocks the entrainment from the bottom. With increase in their extent, the entrainment shifts entirely to the top. When the horizontal surface is held isothermal at the same temperature as that of the vertical one, the entrainment characteristics are entirely different, as shown in Fig. 3, since the buoyancy-induced flows adjacent to both the surfaces now require entrainment.

First, consider the entrainment requirements of the

Table 2. Comparison of Nu for $Ra = 0.7 \times 10^6$, $Pr = 0.7$ and $W^* = 0$

Present	Churchill and Chu [12]	Gebhart *et al.* [9]
15.52	15.53	15.04

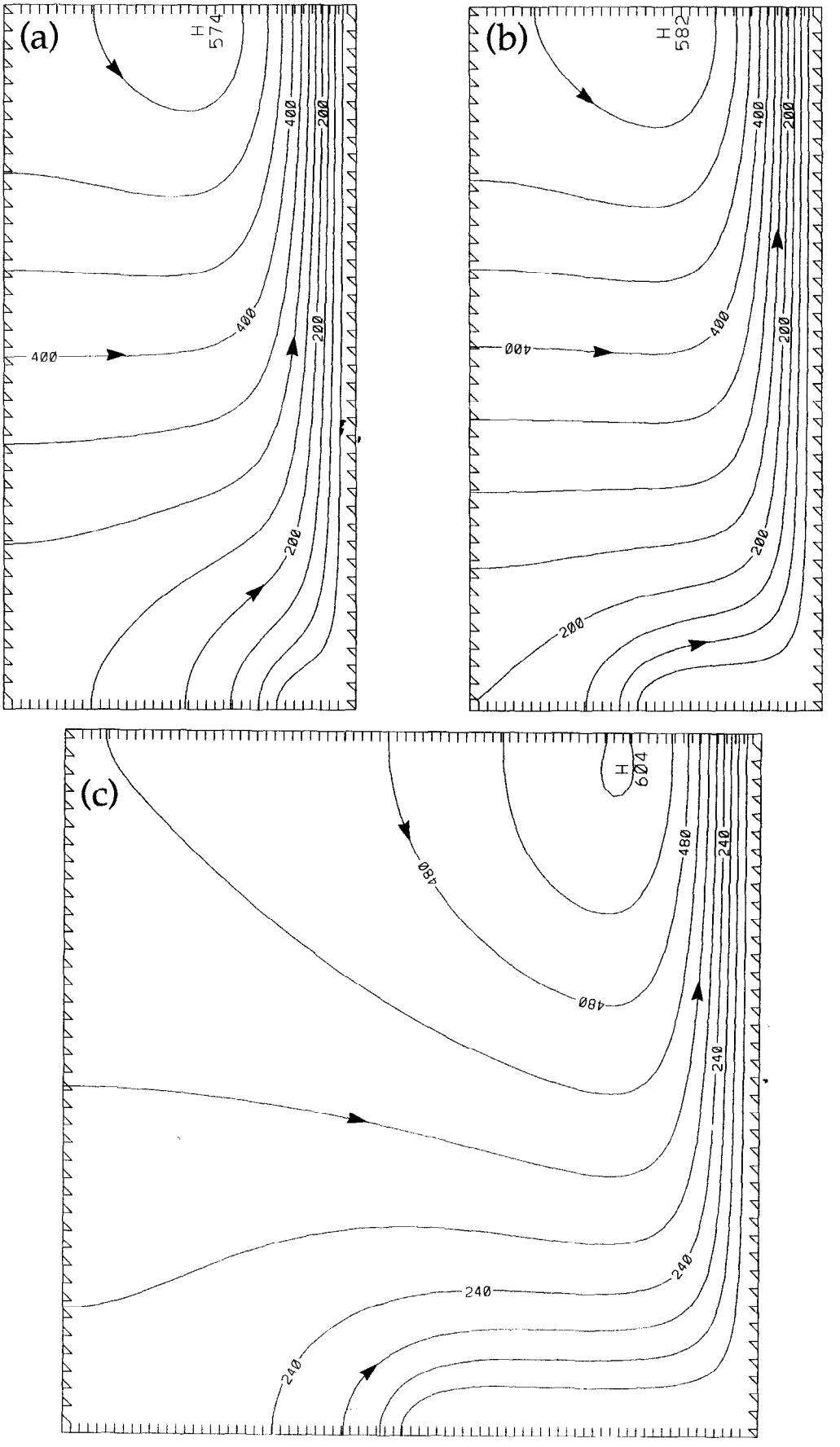

FIG. 3. Stream function contours for $Gr = 10^6$ and $Pr = 0.7$. $\psi_{wall} = 0$. $W^* = 0.1$ (a), 0.25 (b), 0.5 (c), 0.75 (d), 1.5 (e) and 2.0 (f). $\Delta\psi = 50 \times 10^{-4}$ (a, b), 60×10^{-4} (c, d) and 70×10^{-4} (e, f).

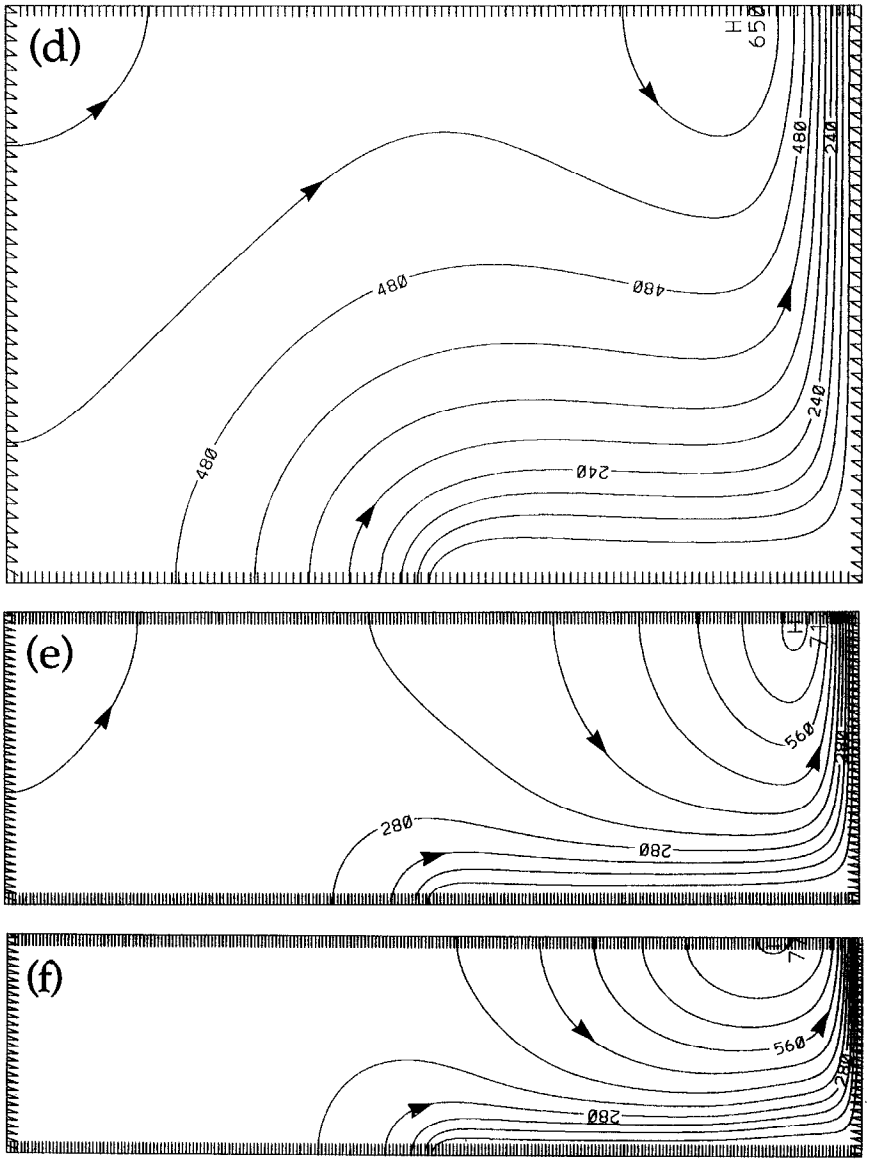

FIG. 3—*continued.*

vertical boundary layer. Although the heated horizontal side blocks the entrainment from the bottom, the buoyancy-driven flow over the horizontal side feeds the vertical boundary layer flow at the corner. If the horizontal extension is short, additional required entrainment is provided from the ambient on the side (Fig. 3(a, b)). With increase in W^*, the entrainment from the side shifts to the top (Fig. 3(c)) until at larger W^* it is almost entirely from the top (Fig. 3(d–f)).

For the horizontal side of the corner, we note that the entrainment fluid is fed from below the surface for all $W^* > 0$. This is quite different from the entrainment characteristics observed for a single horizontal surface (see Ishiguro *et al.* [13] and Angirasa and Mahajan [14]). There, the entrainment is essentially horizontal and from the ambient above the surface. Also, for a single horizontal surface with a plume in the middle, the plume flow has its source of buoyancy only at its origin, which it expends during its growth. On the other hand, the vertical boundary layer flow of the L-shaped corner has a continuous heat supply as it washes the vertical surface. The entrainment for the vertical wall layer is much stronger than for the free boundary plume. Hence, for flow over a single horizontal surface, the entrainments for the horizontal wall flow and for the central vertical plume flow can both be fed horizontally from the side. For the L-corner, on the other hand, the entrainment for the vertical flow is supplied from the side and the top, while the horizontal flow entrains from the bottom.

These entrainment characteristics have an important significance in the choice of computational domain in numerical simulations. Only a domain extended beyond W^* in the Y-direction can include

the entrainment for the horizontal flow from below. A computational domain truncated at W^* entrains fluid from the side for the horizontal flow, while increasing the entrainment velocities for the vertical flow. The result is increased heat transfer rates, as shown in Table 1.

Isotherm contours for various W^* are shown in Fig. 4. For short protrusions, as expected, the flow over the horizontal surface does not exhibit boundary layer characteristics. With increasing W^*, the boundary layer is established. The temperature gradients are weakest in the corner region. Also, there is no plume formation on the horizontal surface at this Rayleigh number, even for $W^* = 2.0$. There is a uniform flow pattern of the fluid washing the horizontal surface and then turning over the corner to form the vertical boundary layer.

The calculated values of Nusselt number as a function of W^* are shown in Fig. 5. The vertical Nusselt number (Nu_v) falls sharply with a short protrusion at the leading edge. Two possible causes are as follows. The first is the considerable reduction in the cold fluid entrainment from the bottom (see Angirasa and Mahajan [1]). The second is the preheating of the fluid as it flows over the horizontal surface, which reduces the temperature gradients on the vertical wall. With increasing W^*, a relatively smaller fraction of entrainment flow is preheated by the horizontal surface. This results in a decrease in Nu_v. When W^* exceeds about 1.0, the entrainment flow for the vertical plate is well established and changes little with further increase in W^*. Correspondingly, Nu_v stays essentially constant. Also shown in Fig. 5 are Nu_h and Nu_L. As expected, Nu_h increases with W^*. The average Nusselt number for the corner, Nu_L, is simply the average of Nu_v and Nu_h.

Effect of Rayleigh number. To study this effect, calculations have been performed for a square corner ($W^* = 1$) and $Pr = 0.7$ for three values of the Grashof number, 10^4, 10^5 and 10^6. Steady-state solutions are obtained for all three Gr values.

In Fig. 6 stream function contours are shown, while Fig. 7 gives the corresponding isotherms. At $Gr = 10^4$, the transport is dominated by diffusion. Also, there is no boundary layer formation at this low Grashof number. As Gr is increased to 10^5, boundary layer type flow can be discerned adjacent to the vertical side. At $Gr = 10^6$, steady boundary layer flows are established over both surfaces.

An interesting aspect to be pointed out here is that while entrainment velocities increase with increasing Grashof number, the sources of entrainment are unaffected by it. It appears that, for this range of Ra, the geometry of the flow configuration determines where the entrainment comes from.

The variation of Nusselt number with Rayleigh number ($Pr = 0.7$) is presented in Fig. 8. At lower Rayleigh number Nu_h is larger than Nu_v, while at higher Ra the trend is reversed. At lower Ra, the vertical boundary layer flow is mostly fed by the preheated fluid from the horizontal flow. Hence the temperature gradients on the vertical leg are lower than those on the horizontal side. The result is a decreased Nu_v. At higher Gr, however, the preheating is more than offset by a larger entrainment of cold fluid from the top into the vertical boundary layer. This substantially increases the heat transfer rate. We recall that at a higher Gr, the vertical boundary layer dominates in capturing the entrainment flow from the top which, in turn, blocks any flow from the side and forces the horizontal flow to entrain from the bottom.

In Fig. 8, comparisons are also made with the Nusselt number of a single vertical plate (Nu_{sv}) and a single horizontal plate (Nu_{sh}). The correlations for these are respectively taken from Churchill and Chu [12] and Lloyd and Moran [15]. In each case, the Nusselt number of the single plate is substantially higher than of the corresponding surface of the L-corner.

As explained earlier, the lower heat transfer rate on the vertical wall of the L-corner is due to the preheating of the fluid as it first flows over the horizontal surface. The reason for smaller Nu_h compared to Nu_{sh} may be due to the lower entrainment for the horizontal plate of the L-corner. Ruiz and Sparrow [8] made measurements in water for a higher range of Rayleigh number than considered here. They found that at the higher end of Ra considered, Nu_h is larger than Nu_{sh}. The possible reason cited for this is an acceleration in the flow over the horizontal surface because of the vertical boundary layer. However, when their results are extrapolated to the lower range of Ra, Nu_h is lower than Nu_{sh}. It is possible that at the high Ra in their experiments the large entrainment of the vertical boundary layer acts as a forced flow imposed over the natural convection horizontal flow. At lower Ra, the imposed forced flow is insignificant over the horizontal surface. The entrainment characteristics, as discussed earlier, seem to suggest that the velocities over the horizontal surface drop at lower Ra.

Unsteady laminar flows

At higher Rayleigh numbers, the numerical calculations for laminar flow resulted in unsteady flow and transport. Ruiz and Sparrow [8] concluded that the flow in their experiments—at least over the horizontal surface—was turbulent. In Fig. 9, transient stream function contours are shown for $Pr = 0.7$ and $Ra = 0.7 \times 10^7$. Figure 10 gives the corresponding isotherms. The initial conditions are given by equation (16). They imply that the corner is impulsively heated from a condition of no flow and no heat transfer. Initially a plume begins to grow at the leading edge of the horizontal plate. This is in sharp contrast to flow over a single horizontal plate, where the plume forms at the mid-plane. In this initial phase, the entrainment for the vertical boundary layer is induced from the top. As the plume at the horizontal leading edge grows, it competes with the vertical wall boundary layer for

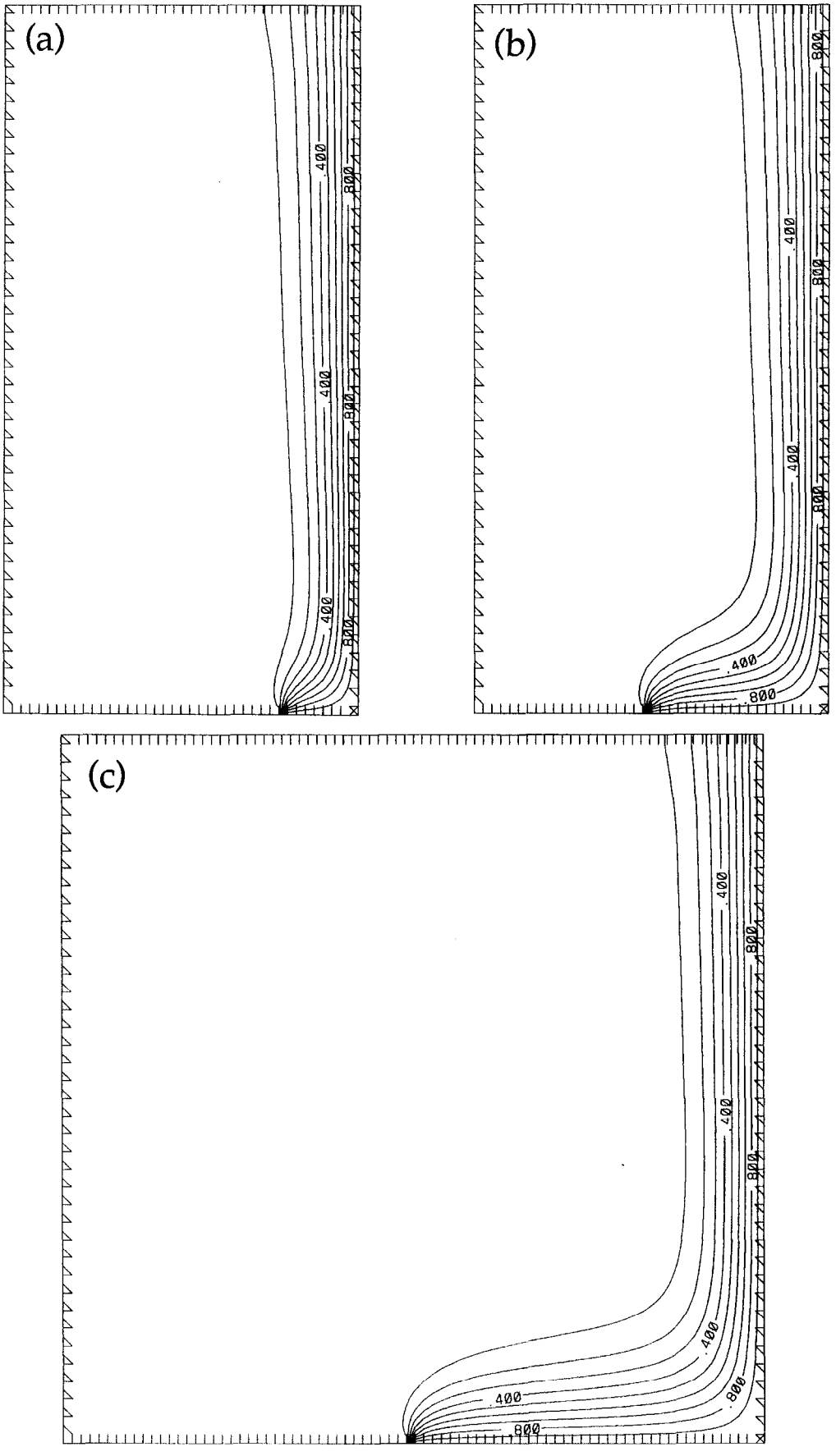

FIG. 4. Isotherms for $Gr = 10^6$ and $Pr = 0.7$. $T_{wall} = 1$ and $\Delta T = 0.1$. $W^* = 0.1$ (a), 0.25 (b), 0.5 (c), 0.75 (d) and 1.5 (e).

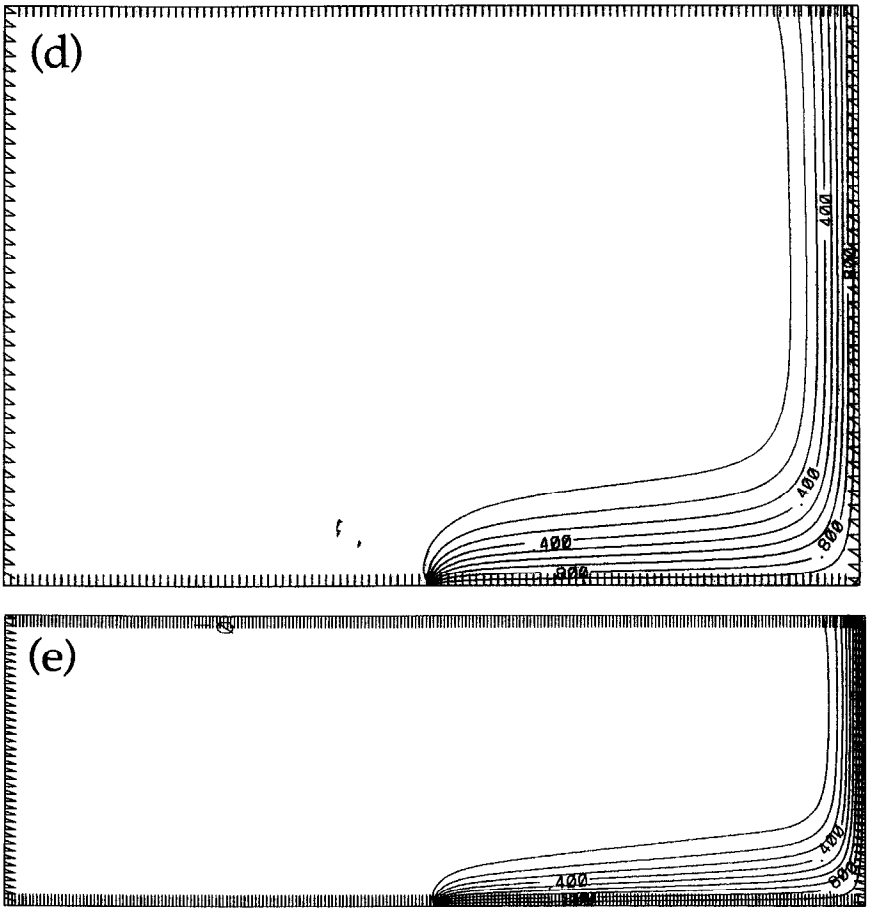

FIG. 4—*continued.*

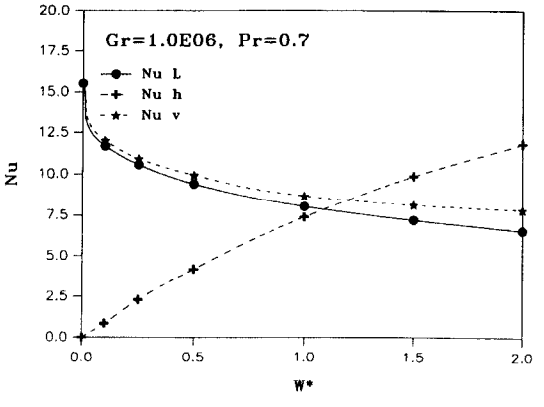

FIG. 5. Variation of Nusselt number with W^* for $Gr = 10^6$ and $Pr = 0.7$.

entrainment from the top. This is clearly illustrated by the clockwise vortex in Fig. 9(b).

Recall that the vertical wall boundary layer is stronger than the vertical free boundary plume. Hence, in the competition for the entrainment from the top, the wall layer wins. The resulting adverse pressure gradient drives the plume towards the wall. The plume ultimately merges with the vertical wall boundary layer (Figs. 9(c, d) and 10(c, d)).

Once the initial rising plume merges with the vertical wall layer, smaller plumes (or 'ripples') continue to form on the horizontal plate, but they cannot rise because, by then, the vertical wall layer is well established and completely dominates the flow. The formation of ripples on the horizontal wall has definite periodicity as they travel along both the horizontal and vertical flows. This is shown in Figs. 9(e–h) and 10(e–h), and more conclusively in the Nusselt number

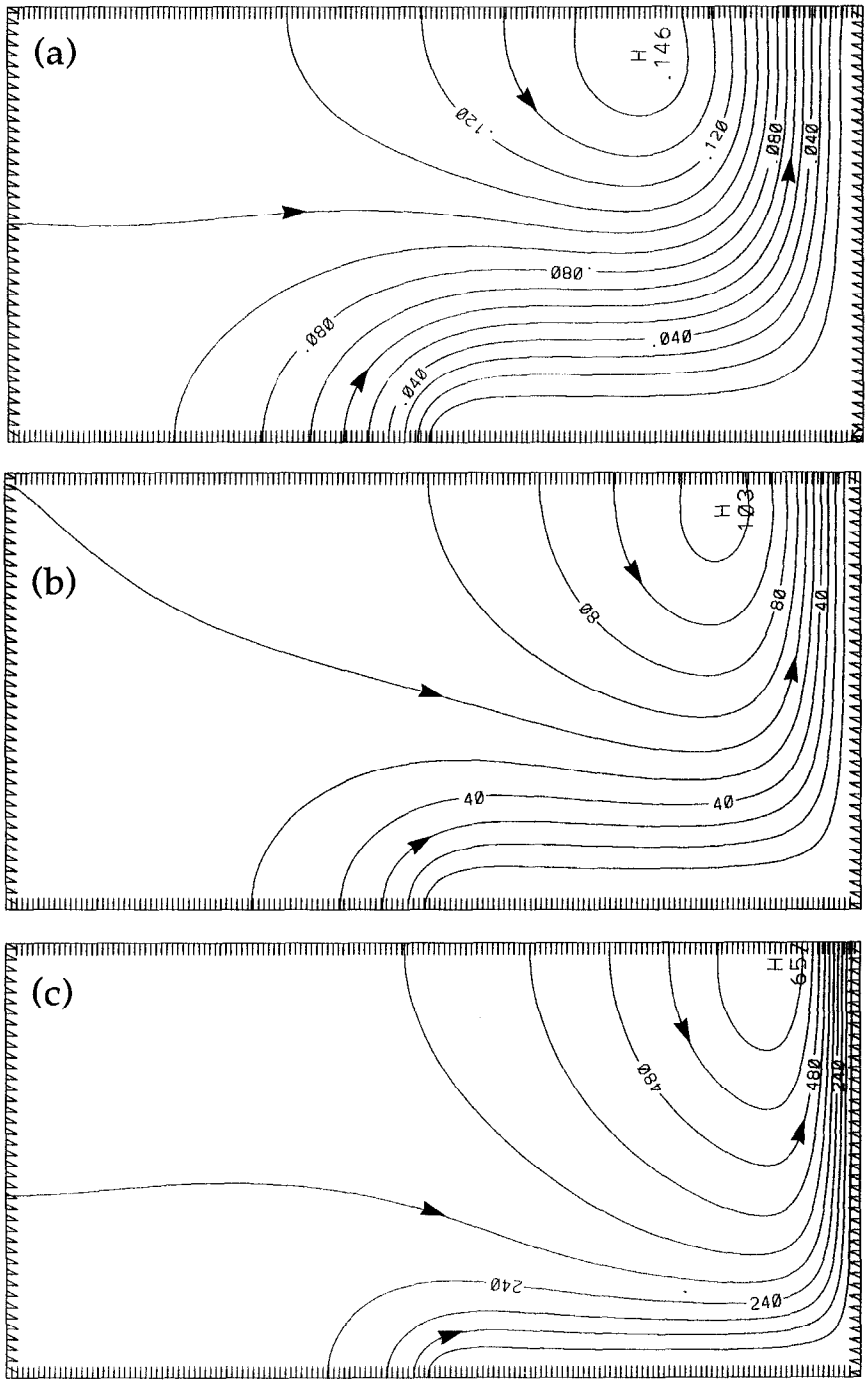

FIG. 6. Stream function contours for $W^* = 1$ and $Pr = 0.7$ at various values of Grashof number. $\psi_{wall} = 0$. (a) $Gr = 10^4$, $\Delta\psi = 0.01$; (b) $Gr = 10^5$, $\Delta\psi = 0.01$; (c) $Gr = 10^6$, $\Delta\psi = 6 \times 10^{-3}$.

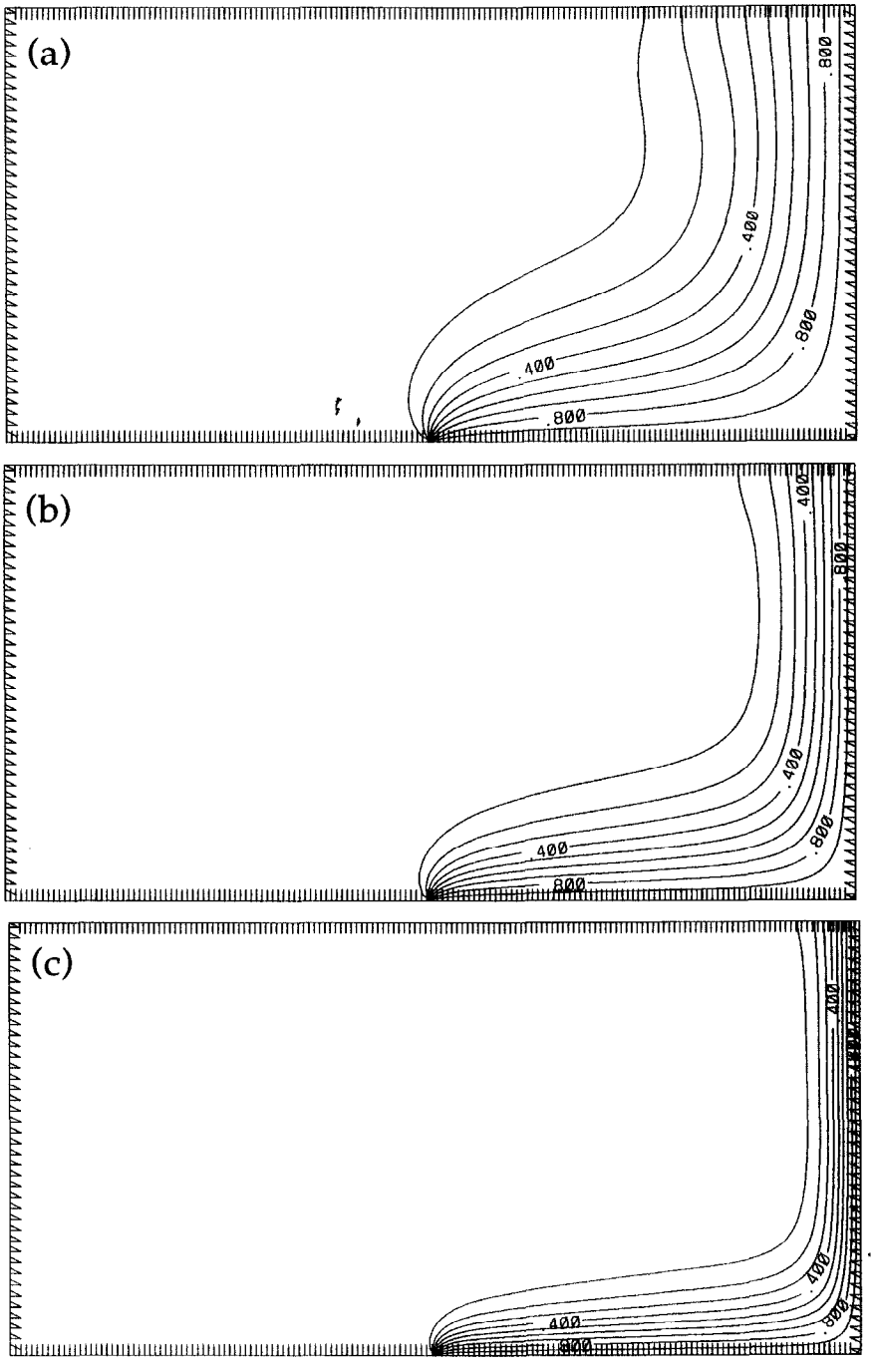

FIG. 7. Isotherms for $W^* = 1$ and $Pr = 0.7$ at various values of Grashof number. $T_{wall} = 1.0$, $\Delta T = 0.1$. $Gr = 10^4$ (a), 10^5 (b) and 10^6 (c).

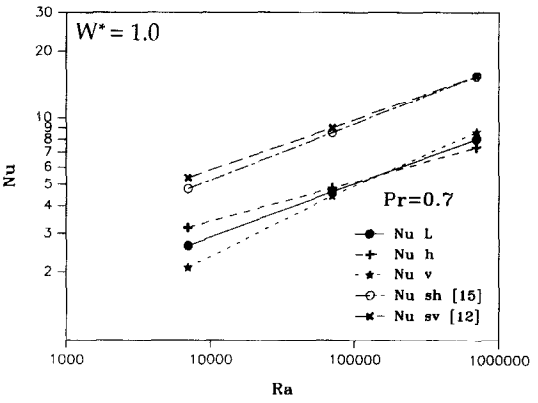

FIG. 8. Variations of Nusselt number with Rayleigh number. L, average for the L-corner; h, horizontal plate of the L-corner; v, vertical plate of the L-corner; sh, single horizontal plate; sv, single vertical plate.

variation with time, as shown in Fig. 11. The variation of the vertical wall Nusselt number has much larger amplitude than that of the horizontal wall. This is to be expected because the ripples formed on the horizontal surface are all fed to the vertical flow, where their compound effect is reflected in the large amplitude of the Nusselt number variation with time.

An intriguing aspect of the transient flow development is the initial formation of the plume at the horizontal leading edge, rather than in the middle of it. For the plume to form in the middle of the horizontal surface, it would have to compete with the stronger vertical wall boundary layer for the entrainment fluid. The best location for the plume to form is the horizontal leading edge, where it can draw entrainment fluid from the ambient, far away from the vertical surface.

Effect of Prandtl number. At $Ra = 0.7 \times 10^7$, the flow and transport for $Pr = 7.0$ are entirely different from those discussed for $Pr = 0.7$. Figures 12 and 13 respectively show transient stream function contours and the corresponding isotherms for $Pr = 7.0$. The initial conditions for this study are the same as those for $Pr = 0.7$. At high Prandtl number, the plume at the horizontal leading edge continues to rise vertically upward (Figs. 12 and 13). Both the vertical wall layer and the free boundary plume establish themselves separately. At $Pr = 7.0$, the thermal diffusion is confined to a narrow region. As a result, the strong interaction between the vertical wall and horizontal leading edge flows observed for $Pr = 0.7$ is absent in this case.

The competing entrainments of the two vertical flows introduce instabilities in the flows. These are manifested in either random swaying of the plume (Figs. 12(f, g) and 13(f, g)), or the creation and transmission of ripples on the horizontal surface (Figs. 12(d, e) and 13(d, e)). The total flow and thermal fields remain unsteady. This behavior is also reflected in the variation of Nusselt number, shown in Fig. 14.

The differences in solutions due to Prandtl number are not confined to unsteady high Rayleigh number flows. Table 3 lists the values of Nusselt number for steady low Rayleigh number flows for $Pr = 0.7$ and 7.0. Even here the differences are substantial. The differences are probably due to the interaction of entrainment flows with unequal thermal diffusion.

It is not possible to compare our numerical results with the experimental measurements of Ruiz and Sparrow [8] because the range of Rayleigh number is different. Their experiments in water covered $0.3 \times 10^7 < Ra < 0.5 \times 10^9$. The flow visualizations and the exponent of Ra in their Nu vs Ra relation indicate that they obtained fully developed turbulent flow in that range of Ra. They also obtained quasi-steady Nusselt numbers. It can be concluded that at the Rayleigh number considered by Ruiz and Sparrow [8], the flows are unsteady turbulent. The present numerical study complements the above work by providing physical and quantitative information for laminar flows at the lower Rayleigh number range.

Finally, it needs to be mentioned that there is no plume growth at the leading edge in the experiments of Ruiz and Sparrow [8]. The reason is not hard to discern. In our comparison of unsteady laminar flows for $Pr = 0.7$ and 7.0, we noted that the higher thermal diffusion for $Pr = 0.7$ disperses the plume. If we consider laminar and turbulent flows for the same Prandtl number (based just on molecular diffusivities), the turbulent thermal dispersion is considerably larger than the molecular one, and this precludes plume growth. In addition, at much higher Ra, the vertical wall layer becomes even stronger and ultimately swallows any plume growth at the horizontal leading edge.

5. SUMMARY

In this article, we reported a numerical study of buoyancy-induced flow and heat transfer from symmetrically heated isothermal L-shaped horizontal corners. The highlights of the study are summarized below.

1. Short heated protrusions at the leading edge of a heated vertical surface reduce the heat transfer rates on the vertical surface due to blocked entrainment from the bottom, and the preheating of the fluid which

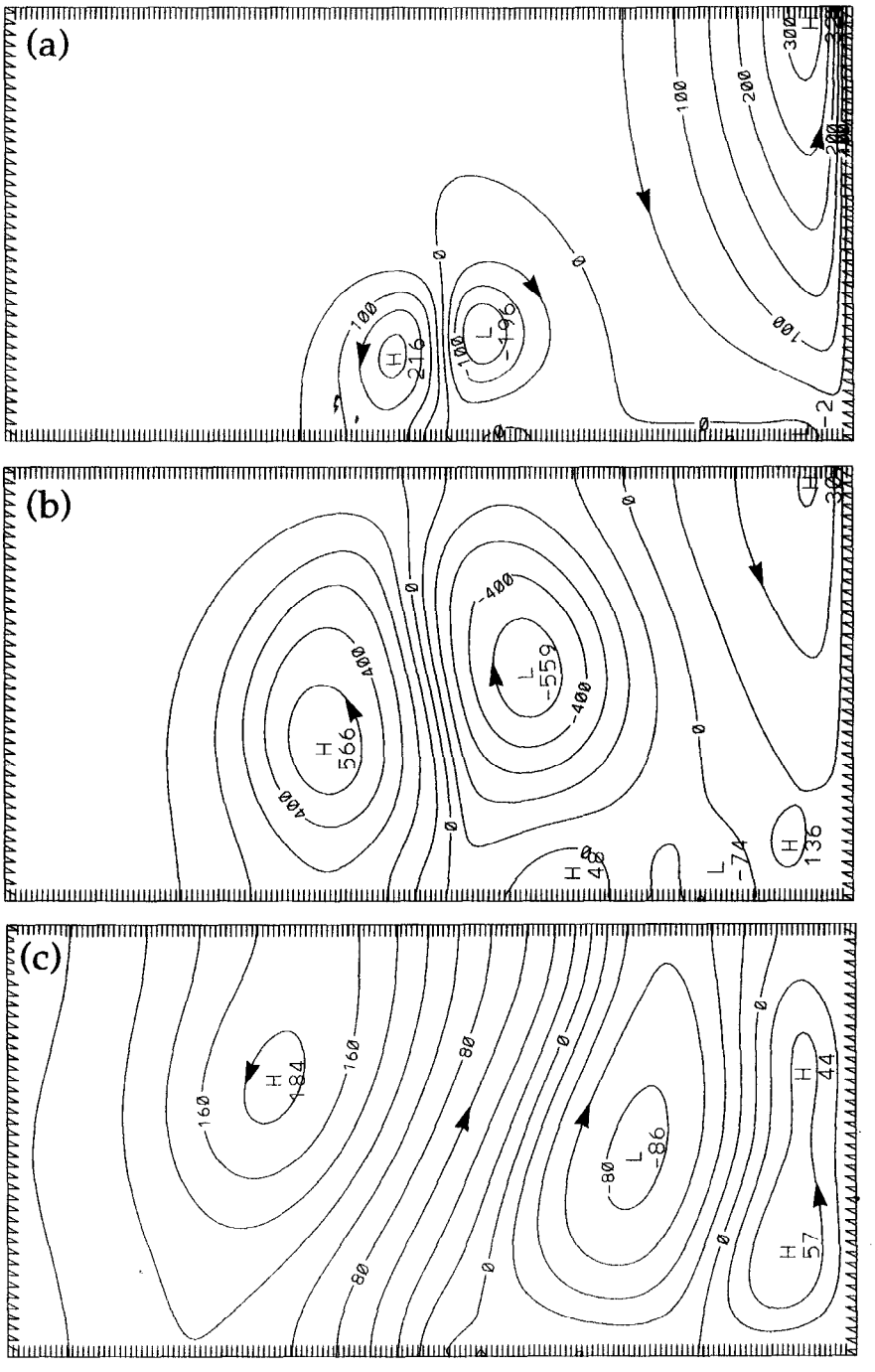

FIG. 9. Transient stream function contours for $Ra = 0.7 \times 10^7$, $Pr = 0.7$ and $W^* = 1.0$. $\psi_{wall} = 0$. $\tau^* = 5$ (a), 10 (b), 25 (c), 40 (d), 55 (e), 80 (f), 90 (g) and 120 (h). $\Delta\psi = 50 \times 10^{-4}$ (a), 100×10^{-4} (b), 20×10^{-3} (c), 10×10^{-3} (d), 10×10^{-3} (e), 80×10^{-4} (f), 80×10^{-4} (g) and 90×10^{-4} (h).

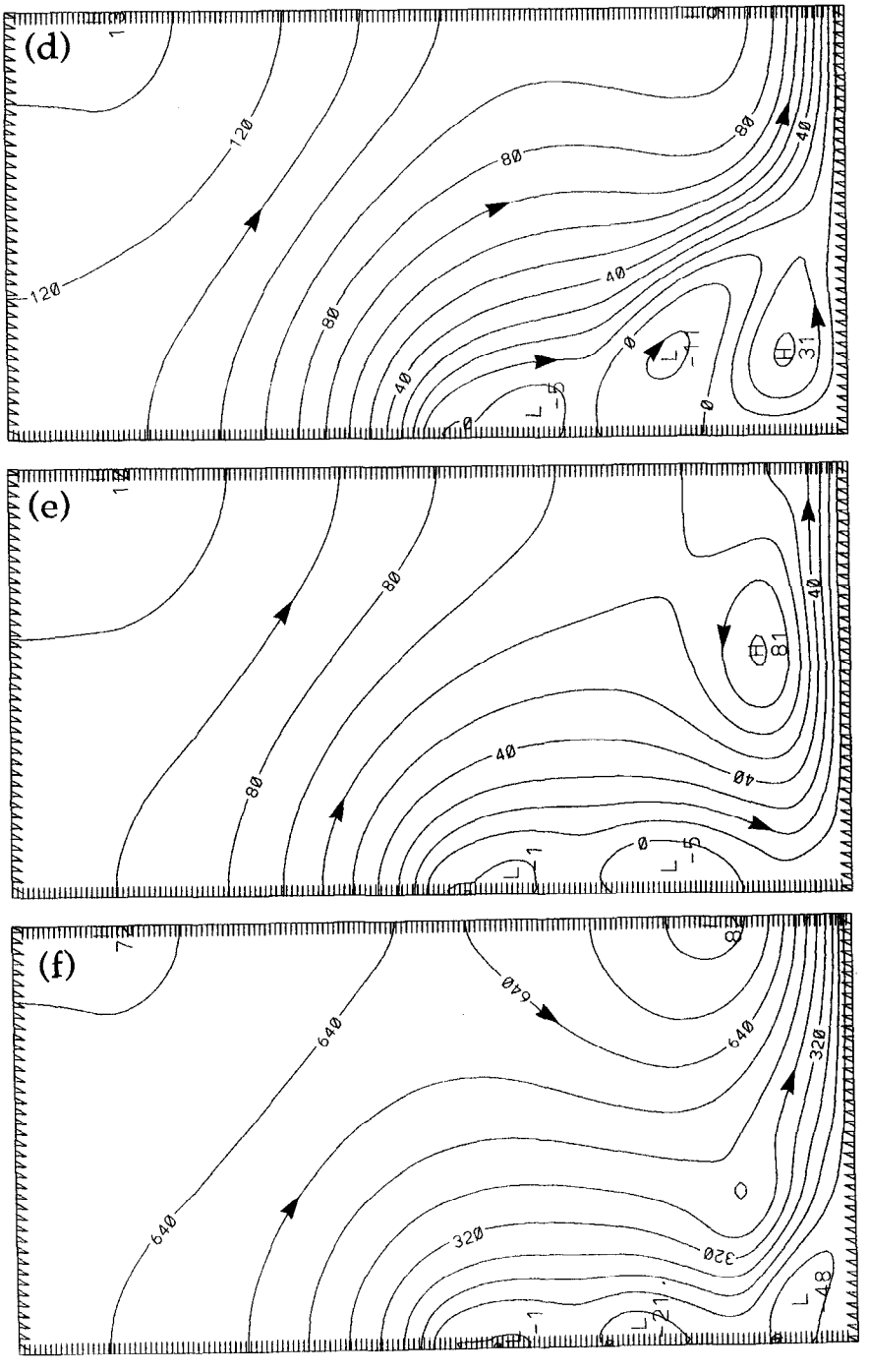

FIG. 9—*continued.*

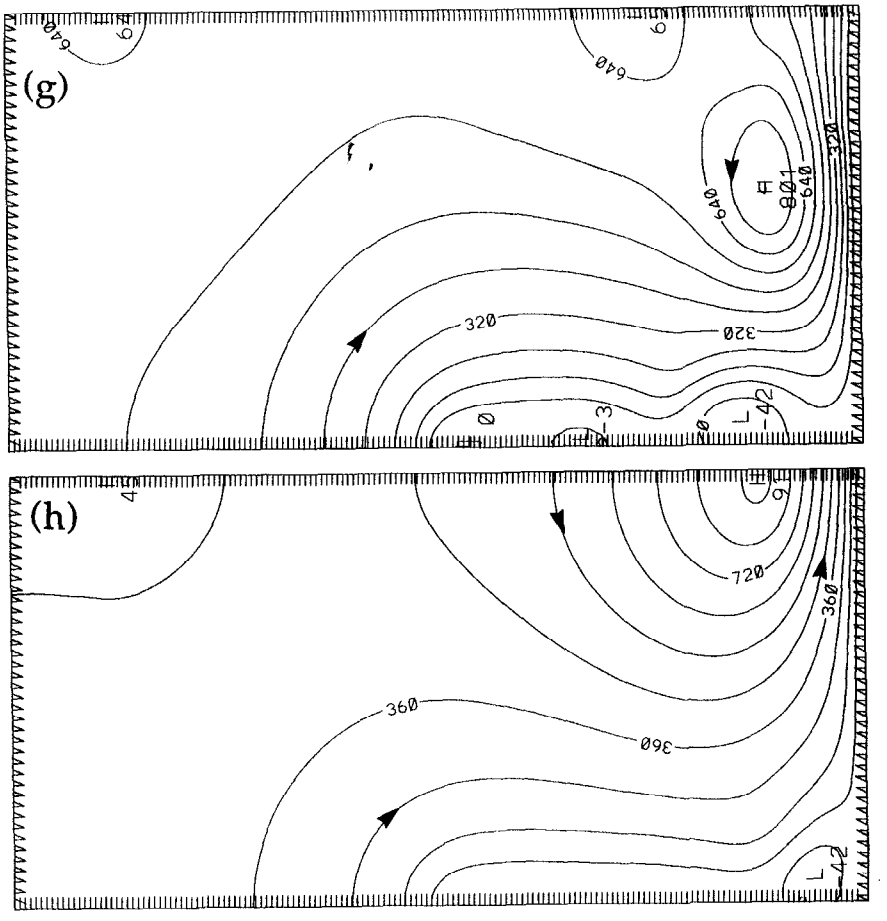

FIG. 9—*continued.*

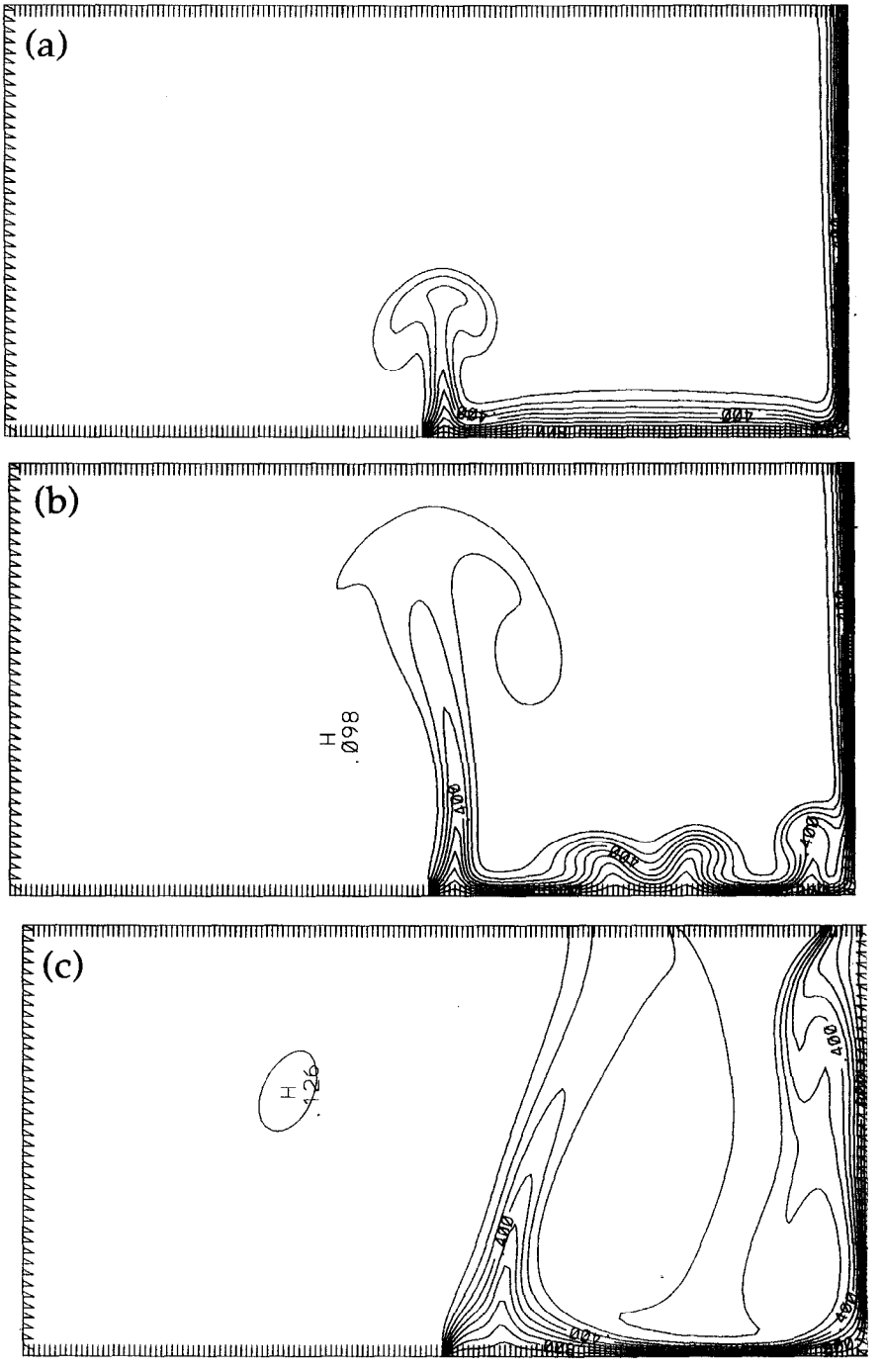

FIG. 10. Transient isotherm contours for $Ra = 0.7 \times 10^7$, $Pr = 0.7$ and $W^* = 1.0$. $T_{wall} = 1.0$ and $\Delta T = 0.1$. $\tau^* = 5$ (a), 10 (b), 25 (c), 40 (d), 55 (e), 80 (f), 90 (g) and 120 (h).

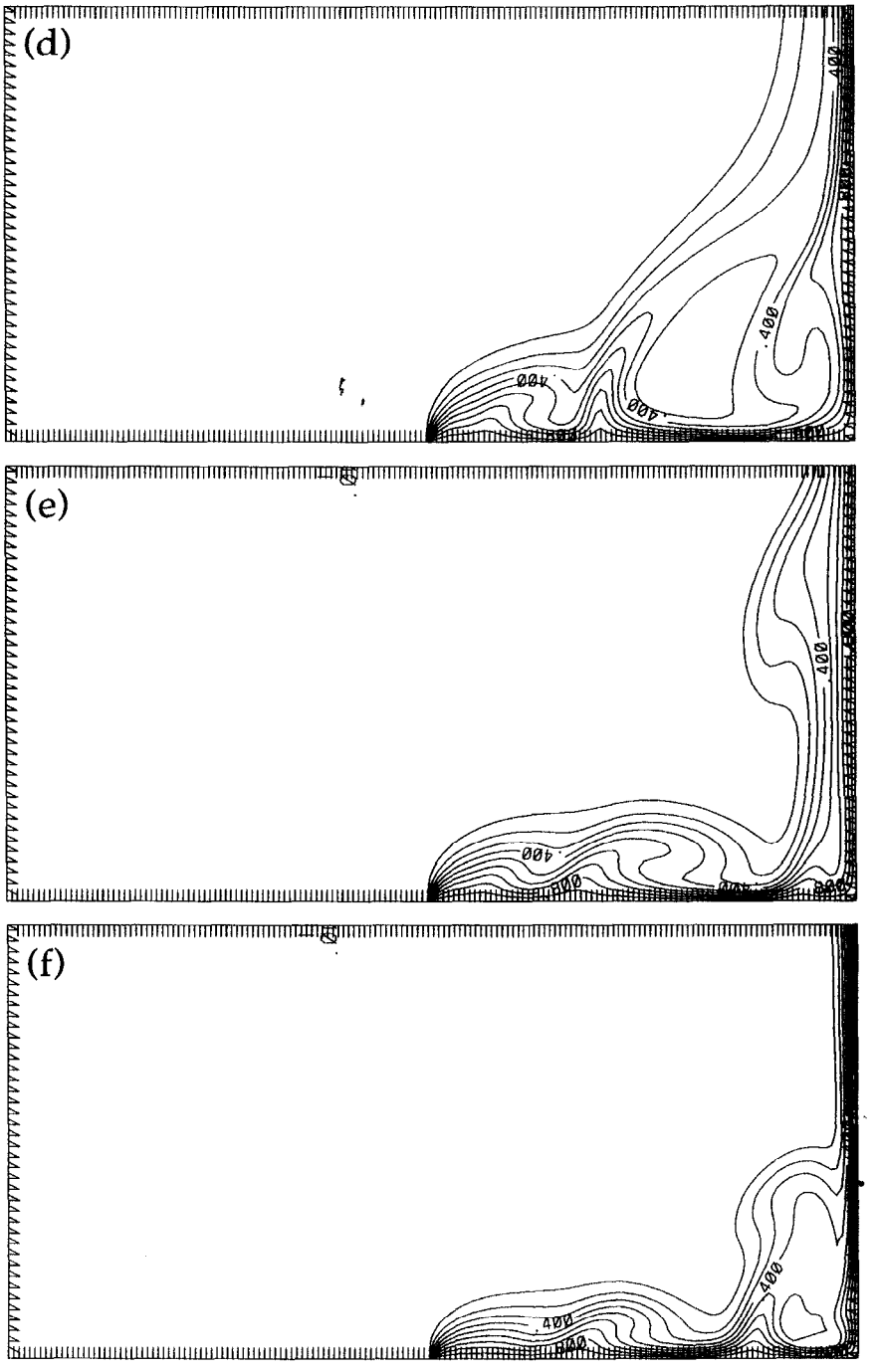

FIG. 10—*continued.*

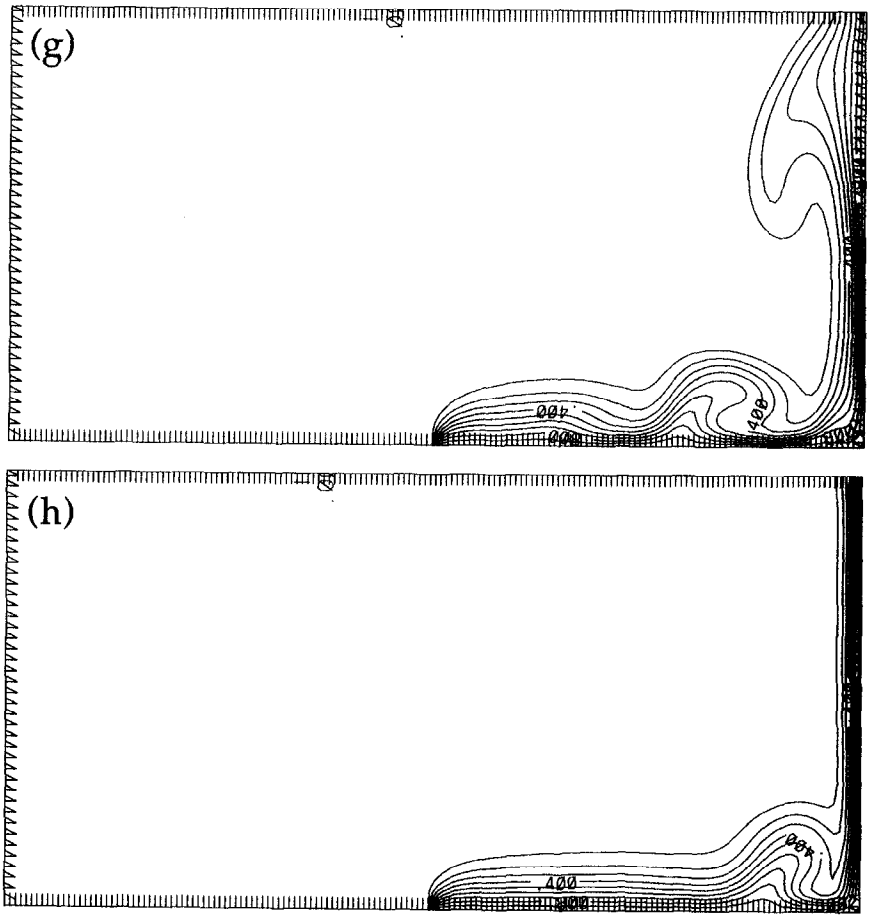

FIG. 10—*continued.*

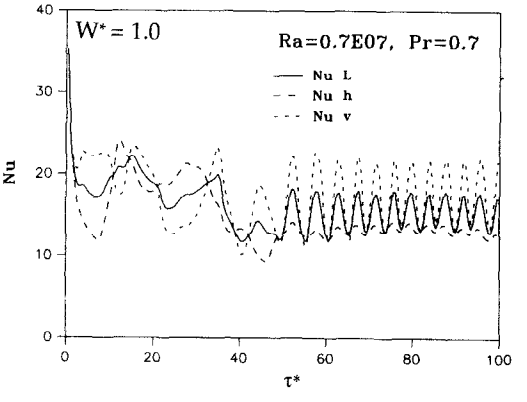

FIG. 11. Nusselt number variation with time for $Ra = 0.7 \times 10^7$, $Pr = 0.7$ and $W^* = 1.0$.

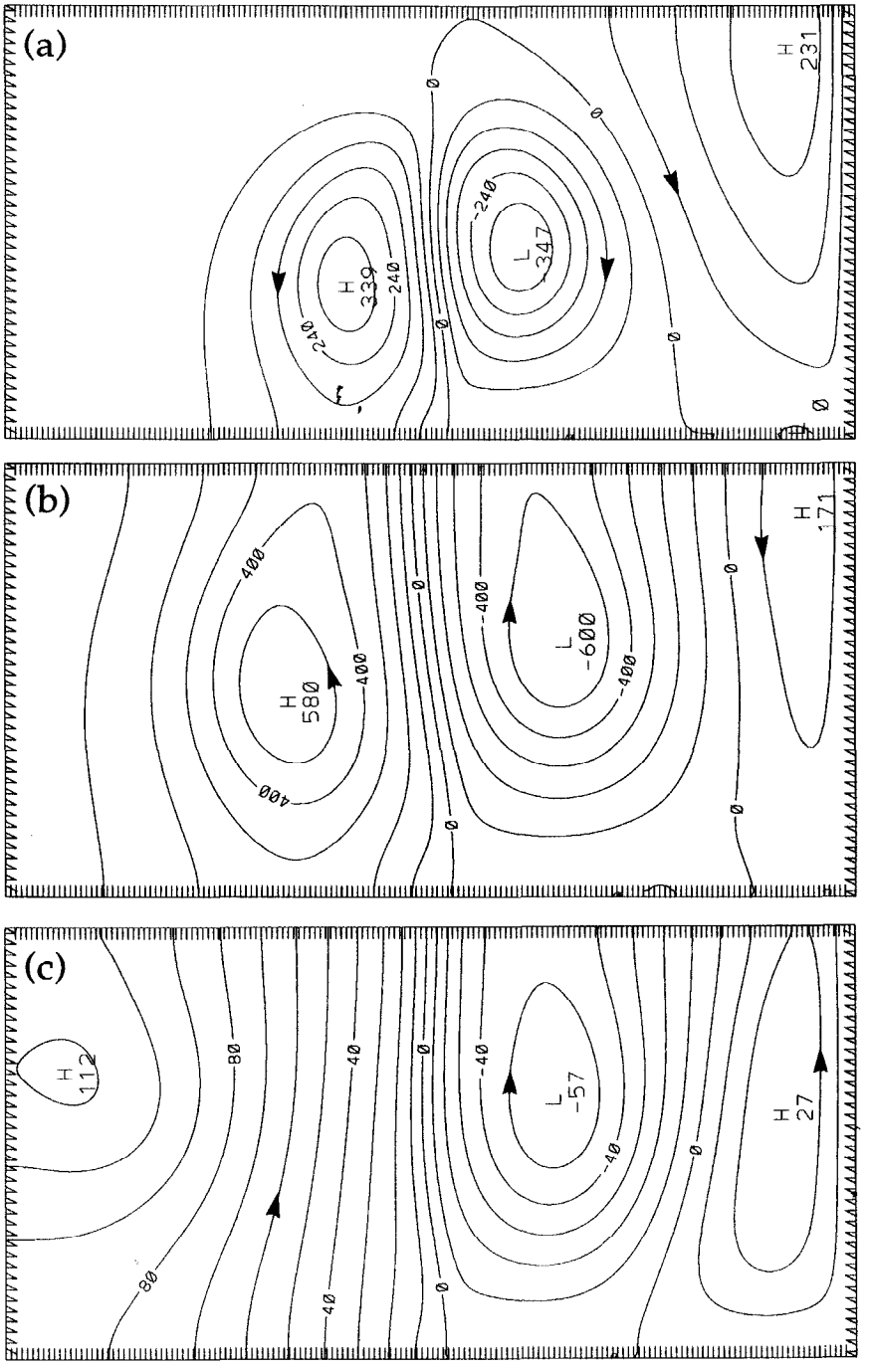

FIG. 12. Transient stream function contours for $Ra = 0.7 \times 10^7$, $Pr = 7.0$ and $W^* = 1.0$. $\psi_{wall} = 0$. $\tau^* = 10$ (a), 15 (b), 35 (c), 75 (d), 80 (e), 90 (f), 100 (g) and 130 (h). $\Delta\psi = 60 \times 10^{-4}$ (a), 10×10^{-4} (b), 10×10^{-3} (c), 70×10^{-4} (d), 60×10^{-4} (e), 70×10^{-4} (f), 90×10^{-4} (g) and 60×10^{-4} (h).

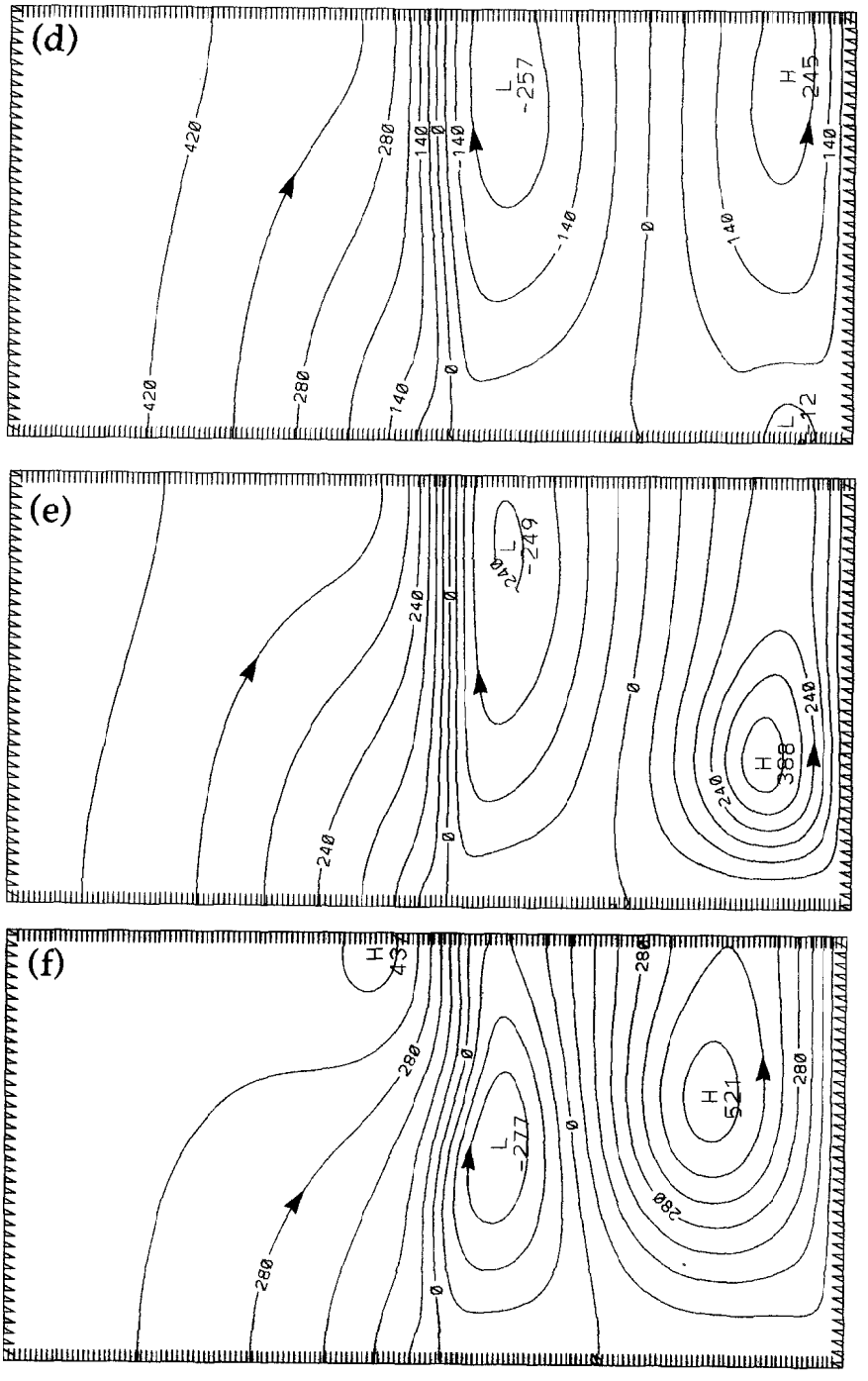

FIG. 12—*continued.*

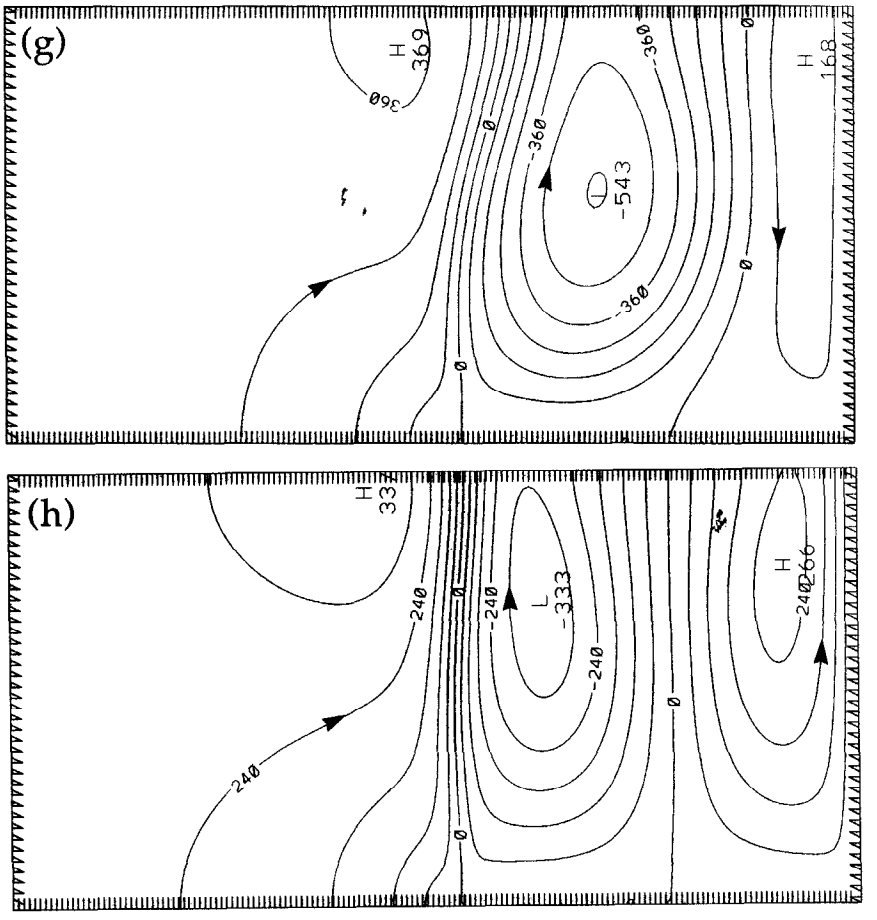

FIG. 12—*continued.*

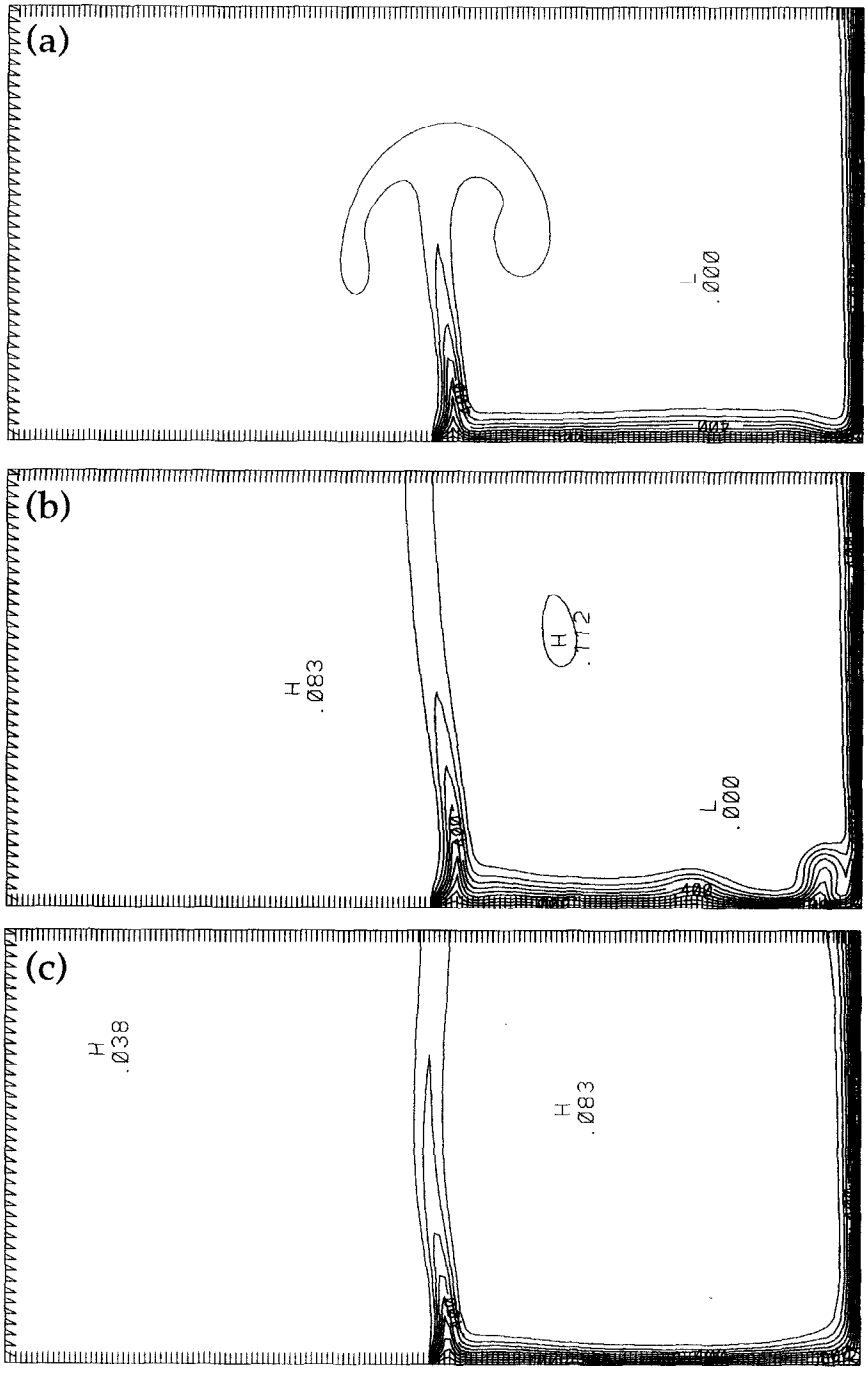

FIG. 13. Transient isotherm contours for $Ra = 0.7 \times 10^7$, $Pr = 7.0$ and $W^* = 1.0$. $T_{wall} = 1.0$ and $\Delta T = 0.1$ $\tau^* = 10$ (a), 15 (b), 35 (c), 75 (d), 80 (e), 90 (f), 100 (g) and 130 (h).

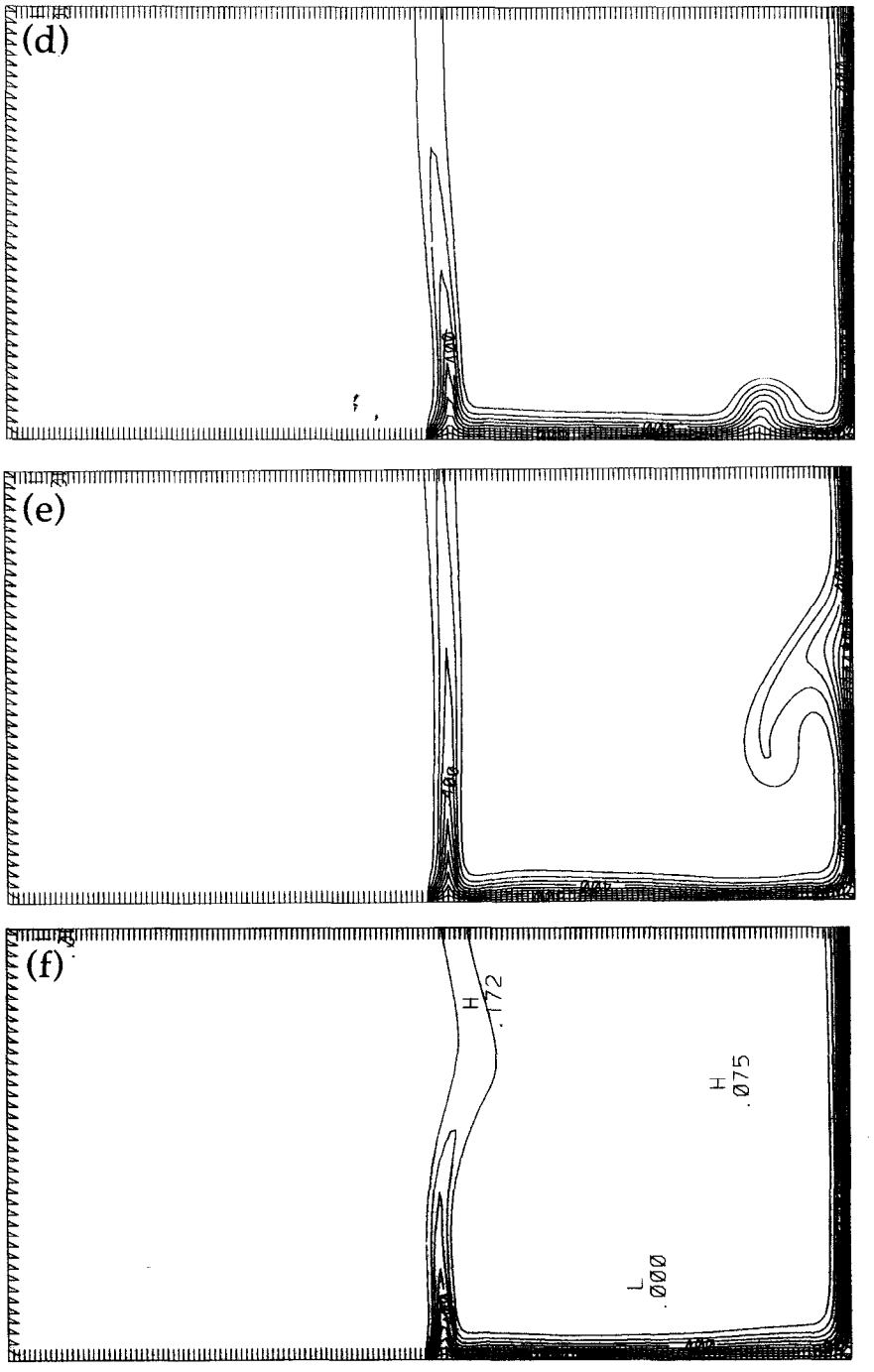

FIG. 13—*continued.*

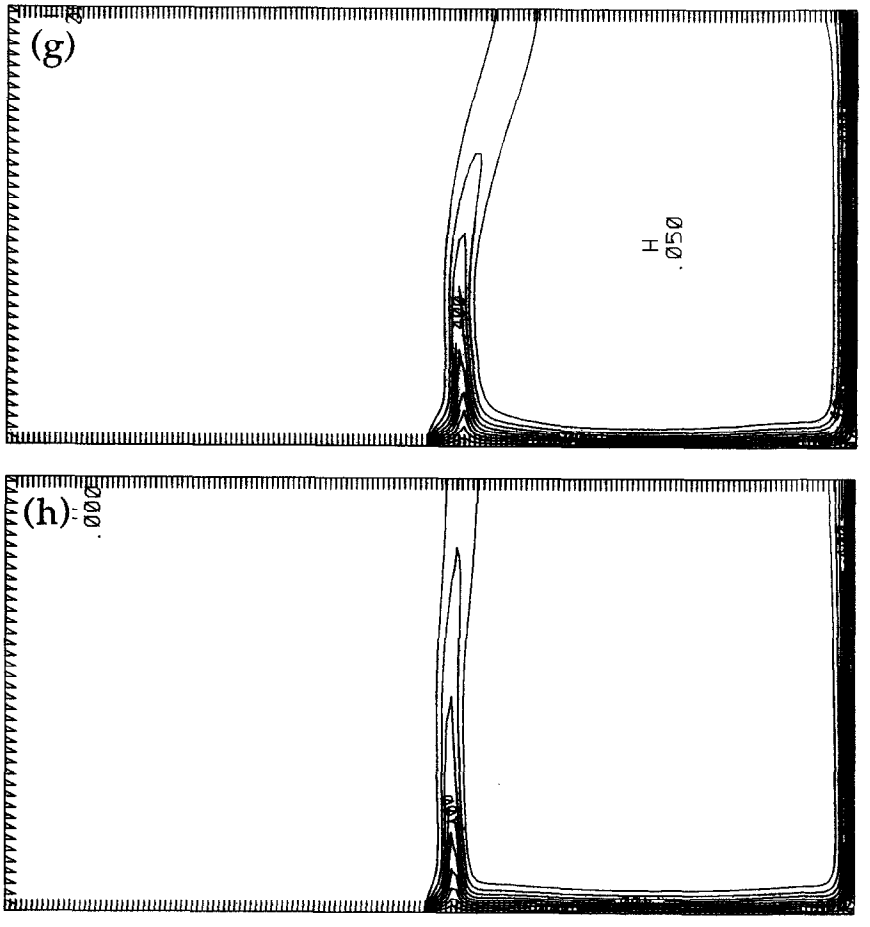

FIG. 13—*continued.*

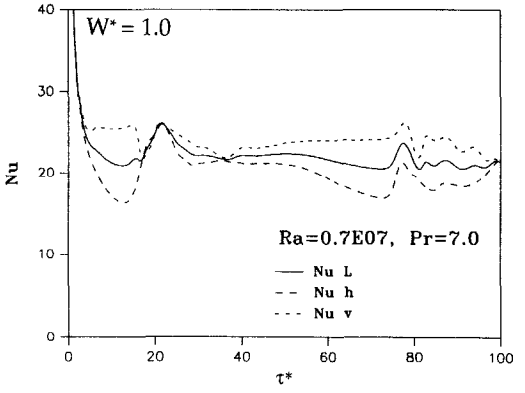

FIG. 14. Nusselt number variation with time for $Ra = 0.7 \times 10^7$, $Pr = 0.7$ and $W^* = 1.0$.

Table 3. Nu for $Ra = 0.7 \times 10^5$ and $W^* = 1.0$

Pr	Nu_h	Nu_v	Nu_L
0.7	4.82	4.45	4.64
7.0	5.67	5.43	5.56

flows over the vertical surface. A further increase in the length of the heated horizontal extension minimally reduces the heat transfer rates on the vertical surface. The heat transfer rates on the horizontal surface expectedly increase with its length.

2. The entrainment characteristics undergo complex changes with an increase in the length of the horizontal surface. The vertical boundary layer entrains from the side, and from the top for short protrusions, and entirely from the top for large horizontal extensions. The horizontal flow entrains from the bottom.

3. The sources of entrainment do not change with an increase in the Rayleigh number as long as the geometric configuration of the flow is unchanged.

4. In the range of Rayleigh number considered here for laminar flows, the Nusselt number for each surface of the L-corner is less than that for the corresponding single surface.

5. At a higher Rayleigh number, the flows are unsteady. For lower Prandtl numbers, there is no plume growth on the horizontal surface, while for higher Prandtl numbers, an unsteady plume develops at the leading edge of the horizontal surface.

6. The Prandtl number has a significant effect on both steady and unsteady flows, independent of the Rayleigh number.

Acknowledgement—This work was partially supported by the National Center for Supercomputing Applications (NCSA) under grant number TRA920487N and utilized the CRAY Y-MP4/464 at the NCSA, University of Illinois at Urbana-Champaign.

REFERENCES

1. D. Angirasa and R. L. Mahajan, Natural convection from L-shaped corners with adiabatic and cold isothermal horizontal walls, *J. Heat Transfer* **115,** 149–157 (1993).
2. C. Rodighiero and L. M. de Socio, Some aspects of natural convection in a corner, *J. Heat Transfer* **105,** 212–214 (1983).
3. D. B. Ingham and I. Pop, Natural convection in a right-angle corner: higher-order analysis, *Int. J. Heat Mass Transfer* **32,** 2167–2177 (1989).
4. D. B. Ingham and I. Pop, A note on free convection flow in a corner, *Int. Commun. Heat Mass Transfer* **15,** 315–321 (1988).
5. D. B. Ingham and I. Pop, A higher-order analysis of natural convection in a corner, *Wärme -und Stoffübertragung* **26,** 289–298 (1991).
6. Y. Jaluria, Interactions of natural convection wakes arising from thermal sources on a vertical surface, *J. Heat Transfer* **107,** 883–892 (1985).
7. P. Luchini, Analytical and numerical solutions for natural convection in a corner, *AIAA J.* **24,** 841–848 (1986).
8. R. Ruiz and E. M. Sparrow, Natural convection in V-shaped and L-shaped corners, *Int. J. Heat Mass Transfer* **30,** 2539–2548 (1987).
9. B. Gebhart, Y. Jaluria, R. L. Mahajan and B. Sammakia, *Buoyancy-induced Flows and Transport*. Hemisphere, Washington, DC (1988).
10. P. J. Roache, *Computational Fluid Dynamics*. Hermosa, Albuquerque, NM (1982).
11. W. H. Press, S. A. Teukolsky, W. T. Vetterling and B. P. Flannery, *Numerical Recipes: The Art of Scientific Computing*, 2nd edn. Cambridge University Press, New York (1992).
12. S. W. Churchill and H. H. S. Chu, Correlating equations for laminar and turbulent free convection from a vertical plate, *Int. J. Heat Mass Transfer* **18,** 1323–1329 (1975).
13. R. Ishiguro, T. Abe, H. Nagase and S. Nakanishi, Heat transfer and flow instability of natural convection over upward-facing horizontal surfaces, *Proc. 6th Int. Heat Transfer Conf.*, Tokyo, Japan, Vol. 2, pp. 229–234 (1978).
14. D. Angirasa and R. L. Mahajan, Combined heat and mass transfer by natural convection over a horizontal surface, *Int. Commun. Heat Mass Transfer* **20,** 279–293 (1993).
15. J. R. Lloyd and W. R. Moran, Natural convection adjacent to horizontal surface of various planforms, *J. Heat Transfer* **96,** 443–447 (1974).